

ARTICLES

Intracellular dynamics of hippocampal place cells during virtual navigation

Christopher D. Harvey^{1,2,3}, Forrest Collman^{1,2,3}, Daniel A. Dombeck^{1,2,3} & David W. Tank^{1,2,3}

Hippocampal place cells encode spatial information in rate and temporal codes. To examine the mechanisms underlying hippocampal coding, here we measured the intracellular dynamics of place cells by combining *in vivo* whole-cell recordings with a virtual-reality system. Head-restrained mice, running on a spherical treadmill, interacted with a computer-generated visual environment to perform spatial behaviours. Robust place-cell activity was present during movement along a virtual linear track. From whole-cell recordings, we identified three subthreshold signatures of place fields: an asymmetric ramp-like depolarization of the baseline membrane potential, an increase in the amplitude of intracellular theta oscillations, and a phase precession of the intracellular theta oscillation relative to the extracellularly recorded theta rhythm. These intracellular dynamics underlie the primary features of place-cell rate and temporal codes. The virtual-reality system developed here will enable new experimental approaches to study the neural circuits underlying navigation.

Hippocampal place cells encode spatial information during navigation using rate and temporal codes^{1,2}. The rate code refers to a selective increase in firing rate at a specific location in a local environment³, and the temporal code includes the precise timing of spikes relative to the hippocampal theta rhythm (phase precession)^{4–6}. To explain the origins of these codes, theoretical network and cellular models have been proposed^{4,7–16}. These models make differing predictions about the subthreshold membrane potential dynamics of place cells (Fig. 1a–e, g–i), reflecting differences in the proposed mechanisms underlying hippocampal coding. The predicted intracellular dynamics include steady oscillations at theta frequencies that reflect a global hippocampal theta rhythm^{7–9,12} (Fig. 1e), modulation of the amplitude and frequency of membrane potential theta oscillations^{4,10,11,13–15} (Fig. 1b–d), and ramps of depolarization of the baseline membrane potential^{7–10,12,13} (Fig. 1d–e). To account for phase precession, these models also make differing predictions about the relationship between intracellular theta oscillations and the local field potential (LFP) theta rhythm. Models predict either that intracellular theta is phase-locked to the LFP theta rhythm with phase precession resulting from a ramp of depolarization^{7–9,12}, or that intracellular theta in the place field is at a higher frequency than the LFP rhythm^{4,10,11,13–15} (Fig. 1g–i).

Because the models of hippocampal coding make differing predictions of subthreshold membrane potential dynamics, it is possible to distinguish between these models by intracellular measurements from place cells during spatial behaviours. However, intracellular recording methods require a level of mechanical stability that is difficult to obtain in freely moving animals^{17,18}. Previously, head restraint on a spherical treadmill has been used to facilitate optical imaging at cellular resolution in awake, mobile mice¹⁹. Furthermore, a previous study has provided evidence that body-tethered rats can navigate through virtual environments²⁰. We reasoned that these could be combined to facilitate whole-cell recordings to show the intracellular dynamics of place cells, and thus distinguish between models of hippocampal coding.

Spatial behaviour in a virtual environment

The visual virtual-reality system for head-restrained mice we developed is shown in Fig. 2a. A mouse runs on top of an air-supported

spherical treadmill with its head held fixed in space using a head plate. The mouse is surrounded by a toroidal screen that covers a wide area to accommodate a rodent's large field of view²⁰. An image is projected onto the screen from a digital light processing projector by an angular amplification mirror²¹ (Fig. 2a, Supplementary Fig. 1 and Methods). To control the virtual-reality system, we developed custom software using the open source Quake2 video game engine. The visual display was updated on the basis of the movements of the animal, measured as rotations of the spherical treadmill using an optical computer mouse (Methods).

We addressed whether head-restrained mice can perform visually guided spatial behaviours in a virtual environment. We trained water-scheduled mice using operant conditioning to run along a virtual linear track (180 cm long) that had proximal and distal walls with varying patterns for location cues (Fig. 2b). Mice were able to turn around at any position along the track's length. Small water rewards were given for running between reward zones located at opposite ends of the track; consecutive rewards were not available at a single reward site. After several training sessions, mice ran large total distances with high peak running speeds (session 4: total distance = 217 ± 97 m per 40 min, peak speed = 41 ± 17 cm s⁻¹ over a 2 s period, mean \pm s.d.). Individual mice received rewards at increasing rates over time (Fig. 2c, d). Also, the average distance travelled between rewards decreased across sessions (Fig. 2e), consistent with learning of the task. After ten training sessions, mice ran 281 ± 53 cm between rewards, on average, approaching an ideal performance of 180 cm per reward (that is, the distance between reward zones). These data indicate that head-restrained mice can perform visually guided spatial behaviours in a virtual-reality environment.

Place cells in a virtual environment

Although our behavioural results indicate that mice have a spatial understanding of the virtual environment, the activation of navigation circuits during these behaviours would provide further evidence. To assess the function of the hippocampal place-cell circuitry, we performed acute extracellular recordings in the dorsal hippocampus from CA1 pyramidal neurons (Fig. 3a). We recorded during behaviour along the virtual linear track from mice that had been trained

¹Princeton Neuroscience Institute, ²Lewis-Sigler Institute for Integrative Genomics, ³Department of Molecular Biology, Princeton University, Princeton, New Jersey 08544, USA.

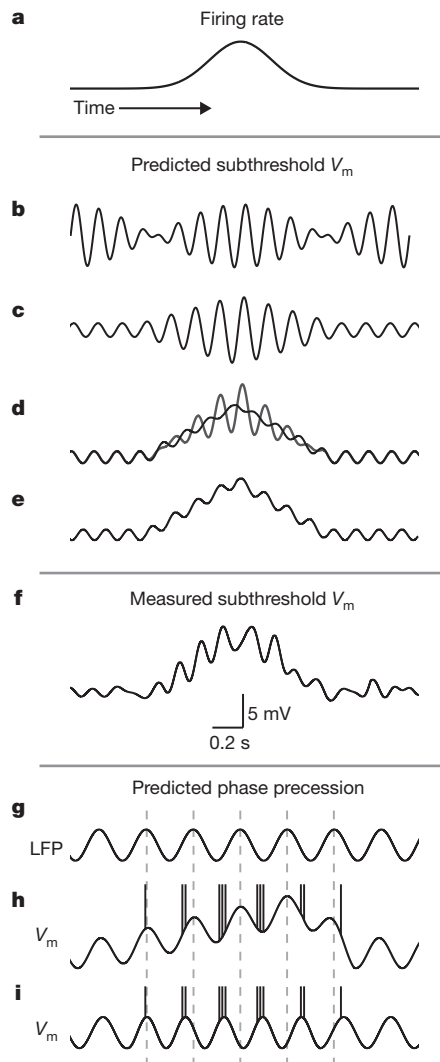


Figure 1 | Predicted and measured subthreshold membrane potential dynamics during a run through a cell's place field. **a**, Schematic of a place-cell's firing rate. **b–e**, Schematics of predicted subthreshold membrane potentials (aligned to **a**) from a dual oscillator interference model^{2,4} (**b**), a modified dual oscillator model¹⁴ (**c**), a soma-dendritic interference model^{10,11,13,15} (**d**), and network^{7–9} and experience-dependent¹² models (**e**). In **b**, two sets of theta-modulated inputs at different frequencies interfere to create a beat-like pattern of membrane potential fluctuations. In **c**, two oscillations are phase-locked outside the place field. In the place field, the frequency of one oscillation increases, resulting in a modulation of the summed oscillation. In **d**, the cell receives theta-modulated inhibitory and excitatory inputs. In the place field, the excitatory drive increases, resulting in a ramp-like depolarization and an increase in the amplitude of excitatory theta oscillations. Depending on the conductances used, the summed oscillation can have either increased (grey)¹⁵ or decreased (black)¹¹ amplitude. In **e**, a ramp of excitatory drive interacts with theta-modulated inhibitory inputs. Asymmetric ramps have also been proposed¹². Schematics in **b–e** only illustrate depolarizations and changes in theta amplitude. **f**, Example of a subthreshold membrane potential (filtered from DC–10 Hz) recorded intracellularly from a place cell. Note the simultaneous ramp of depolarization and increase in theta oscillation amplitude. Scale bars refer to the experimentally measured trace only. **g**, Schematic of the LFP theta rhythm. Dashed lines denote peaks. **h–i**, Schematics of predicted relationships between intracellular and LFP theta to account for phase precession. In **h**, intracellular and LFP theta are the same frequency. Phase precession of spikes occurs relative to both intracellular and LFP theta owing to a ramp of depolarization^{7–9,12}. An asymmetric ramp is shown. In **i**, intracellular theta in the place field is a higher frequency than LFP theta. Spikes precess relative to LFP theta but not intracellular theta^{2,4,10,11,13–15}. Schematics in **h** and **i** only illustrate the relationships between spike times, intracellular theta and LFP theta.

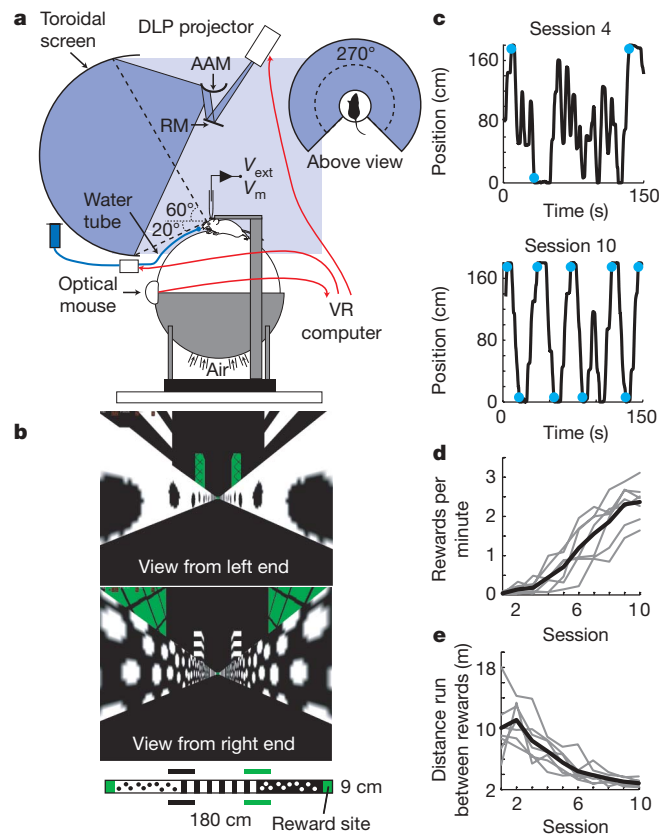


Figure 2 | Spatial behaviours in a virtual-reality environment. **a**, Schematic of the experimental set-up. A head-restrained mouse runs on an air-supported spherical treadmill. An image from a digital light processing projector is displayed on a toroidal screen (−20–60° vertically, 270° horizontally) by a reflecting mirror (RM) and an angular amplification mirror (AAM). Movements of the treadmill are measured using an optical computer mouse. Water rewards are delivered through a lick tube by a computer-controlled solenoid valve. See Methods and Supplementary Fig. 1 for details. **b**, The virtual linear track. Screenshots (without the fisheye perspective, see Methods) from the right and left ends of the track are shown. The track (180 × 9 cm) was divided into three regions with different textures on the proximal walls (black dots, vertical stripes, white dots). Distal walls (horizontal stripes, green with black crosses) were present at the boundaries between regions. Water rewards were given at the ends of the track, with available rewards alternating between reward sites. **c**, Example trajectories for an individual mouse on training sessions 4 and 10. Position is the animal's location along the track's long axis. Blue dots indicate rewards. **d**, Rate of rewards for individual mice. **e**, Average distance travelled by the mouse between consecutive rewards. In **d** and **e**, grey lines indicate individual mice, and the black line is the mean; $n = 7$ mice.

for at least 5 days. Recorded cells had spiking patterns characteristic of hippocampal pyramidal neurons. Cells fired bursts of action potentials at high frequencies (>50 Hz) with decreasing spike amplitudes^{22–24}; bursts occurred at intervals of ~130 ms corresponding to theta frequencies of ~6–10 Hz (Fig. 3a, b). In all mice tested, we identified units with place-cell characteristics (23 cells from 8 mice; Methods). Place cells had low overall firing rates with spatially modulated firing patterns (overall firing rate = 1.0 ± 0.3 Hz; in-field firing rate = 4.7 ± 2.6 Hz; out-of-field firing rate = 0.6 ± 0.2 Hz; Fig. 3c). Place field size was, on average, 41 ± 14 cm. Place-cell activity in some cases had directionality, with different place fields and firing rates depending on the direction of running²⁵ (directionality index = 0.6 ± 0.2 ; Methods and Fig. 3c). We also measured phase precession of spike times relative to LFP theta oscillations during runs through the place field^{4,5}. Spike times shifted to earlier phases during movement through the place field, and the phase and position of spikes were negatively correlated ($\Delta\text{phase} = -72.6 \pm 47.7^\circ$

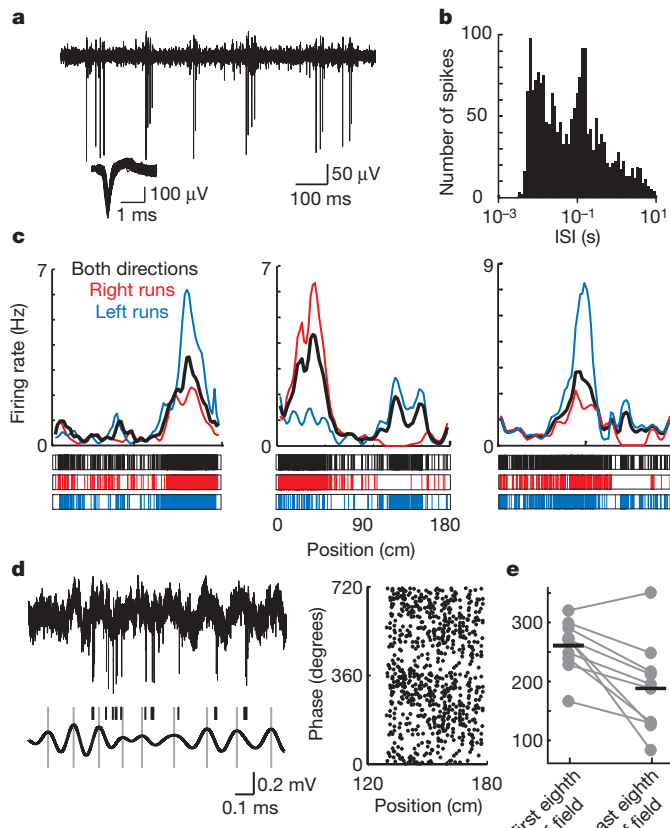


Figure 3 | Extracellular recordings of CA1 place cells along the virtual linear track. **a**, An example extracellular recording filtered between 500 Hz and 7.5 kHz. The inset shows overlaid spike waveforms from the recording. **b**, ISI distribution for the full duration of the recording shown in **a**. The time axis is plotted on a log scale. **c**, Example firing rate maps for 3 place cells from 3 different mice. Top, firing rates at positions along the track are shown for rightward runs (red), leftward runs (blue) and runs in either direction (black). Bottom, the position on the track of each spike in the recording is shown as a vertical line. A total of 23 place cells from 8 mice were recorded. **d**, Phase precession of spike times relative to LFP theta. Top left, an example extracellular recording, filtered between 2 Hz and 10 kHz, during a run through the place field. Spikes and the LFP were recorded on the same electrode. Bottom left, the extracellular recording band-pass filtered between 6 and 10 Hz. Grey lines denote peaks (0°) in the filtered trace, black lines denote the times of spikes. Right, an example plot of phase (two cycles) versus position on the virtual track for all spikes during complete runs through the place field for a single cell. **e**, Phase values for spikes in the first and last eighth of the place field. Connected points represent a single place field. Horizontal lines indicate the means. $n = 10$ place fields from 8 cells and 3 mice (multiple place fields are owing to the directionality of firing rates).

between the first and last eighth of the field, $P < 0.01$; correlation coefficient (C) = -0.17 ± 0.09 between phase and position, $P < 0.01$; $n = 10$ place fields, 8 cells, 3 mice; Fig. 3d, e). These firing rate and phase precession characteristics along the virtual linear track are highly similar to those measured in freely moving mice in real environments^{26–29}. These data therefore demonstrate that hippocampal place-cell circuitry is operational in head-restrained mice during visually guided spatial behaviours in the virtual-reality system.

Intracellular dynamics of place cells

We next developed methods to measure the intracellular activity of hippocampal neurons during behaviour along the virtual linear track. Because the mouse's head is stationary in the virtual-reality set-up, we were able to perform whole-cell patch-clamp recordings using a patch electrode with a long taper mounted on a standard micromanipulator positioned outside the mouse's field of view (see Methods). We obtained recordings in awake mice^{17,18,30,31} as they

ran on the spherical treadmill. Recordings lasted many minutes on average (7.7 ± 3.8 min, maximum 20.4 min; $n = 46$ cells from 15 mice), during which time mice ran long distances at high speeds in the virtual environment (27 ± 5 m per min; total distance range 125–458 m). We did not detect any major motion-induced artefacts in the electrophysiology recordings. Recordings could be performed from the same animal across several days (≥ 6 days per mouse; ≥ 3 days per hemisphere).

A subset of our whole-cell recordings was made from place cells (overall firing rate = 2.2 ± 0.4 Hz; in-field firing rate = 7.3 ± 1.4 Hz; out-of-field firing rate = 1.5 ± 0.4 Hz; field size = 43 ± 13 cm; $n = 8$ cells from 8 mice; Fig. 4a, b and Supplementary Figs 2a and 3). Approximately 36% of the spontaneously active putative pyramidal neurons had a place field along the virtual track, which is consistent with estimates from extracellular recordings and immediate early

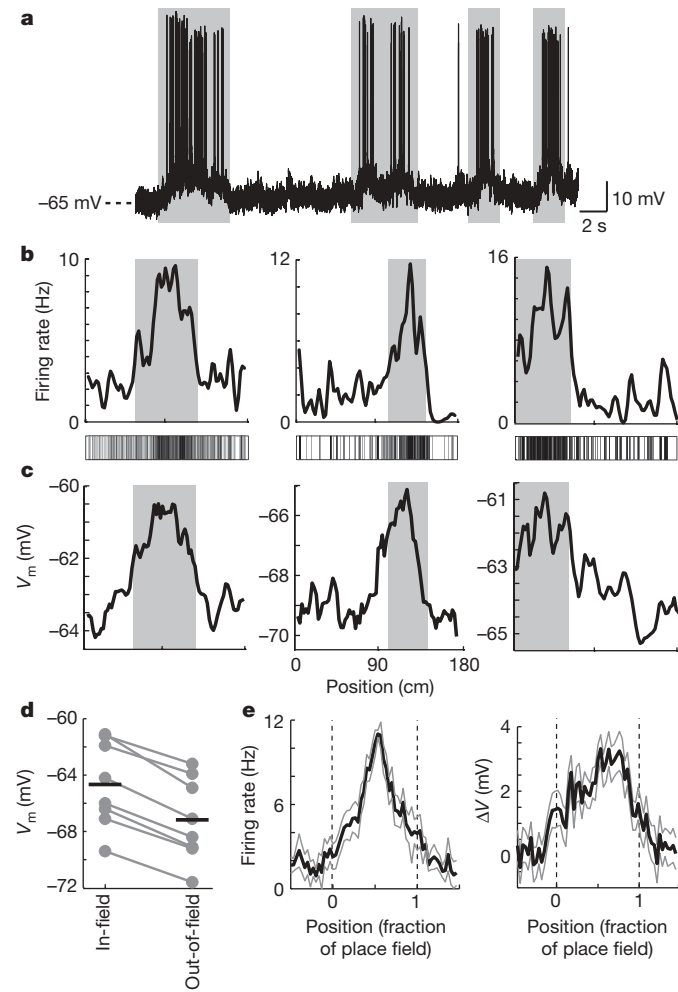


Figure 4 | Ramp-like membrane potential depolarization inside place fields. **a**, Example whole-cell recording during runs through the cell's place field. Grey boxes indicate the place field (middle example from **b**). **b**, Firing rates along the virtual linear track for 3 place cells recorded intracellularly from 3 different animals. The grey boxes indicate the primary place field determined by firing rates (Methods). Bottom, vertical lines mark the location along the track of every action potential in the recording. **c**, Average baseline membrane potential, excluding action potentials, sorted by position along the track for the 3 place cells from **b**. **d**, Average membrane potential inside and outside the place field. Each pair of connected points is from a single cell. Horizontal lines indicate the means. $n = 8$ cells from 8 mice. **e**, Average firing rates and changes in baseline membrane potential during complete runs through the place field. To combine data from several cells, position values in the place field were normalized. Black lines indicate the mean. Grey lines indicate the mean \pm s.e.m. Data are averaged over 84 complete runs through the place field (8 cells).

gene studies in rats exploring real environments^{32,33} (see Methods). Place cells recorded intracellularly fired in theta bursts (high frequency bursts at >50 Hz occurring at theta frequencies of ~6–10 Hz), resulting in interspike interval (ISI) distributions with peaks at <10 ms and ~130 ms, consistent with our extracellular measurements (compare Supplementary Fig. 4 and Fig. 3b). The individual action potentials during a theta burst often occurred during the ascending phase of an underlying theta oscillation (Fig. 5a, d). Spike amplitudes decreased within a burst without a change in the peak potential of the spike, suggesting that depolarizing intracellular oscillations contribute to intra-burst decreases in spike amplitude³⁴. Whole-cell recordings from place cells can therefore be obtained in head-restrained mice behaving in virtual environments.

From our whole-cell recordings of place-cell activity, we examined two types of membrane potential dynamics proposed by the theoretical models of place-cell function: ramps of depolarization, and modulation of theta oscillations (Fig. 1b–e, h–i). We first analysed changes in the average baseline membrane potential during behavioural epochs inside and outside the place field. As a mouse approached the recorded cell's place field, the average membrane potential, excluding action potentials, increased in a ramp-like manner and remained increased until the place field was passed (Fig. 4a). The ramp of depolarization often began before action potential firing in the place field started, and in some cases reached a steady depolarization as large as ~10 mV (peak depolarization = 5.7 ± 2.9 mV; Fig. 4a and Supplementary Figs 5 and

6). These depolarization events occurred preferentially in place fields; the average membrane potential excluding action potentials was higher in place fields than outside of place fields ($V_{\text{in-field}} - V_{\text{out-of-field}} = 2.5 \pm 0.5$ mV, $P < 0.0001$; Fig. 4c, d and Supplementary Fig. 2b). Consistently, the baseline membrane potential and firing rate were strongly correlated ($C = 0.55 \pm 0.10$, $P < 0.001$). On complete runs through the place field, ramps of depolarization were asymmetric, with the peak depolarization shifted towards the end of the field (position of the peak depolarization = $72 \pm 24\%$ of the distance through the field, $P < 0.05$ versus 50%; slope before peak = 3.0 mV per place field length, slope after peak = 5.4 mV per field length, $P < 0.001$; Fig. 4e). In contrast, firing rates were symmetric within the place field (position of the peak firing rate = $52 \pm 17\%$ of the distance through the field, $P > 0.6$ versus 50%; slope before peak = 13.3 Hz per place field length, slope after peak = 13.6 Hz per field length, $P > 0.4$; Fig. 4e), perhaps because firing rates were highest on the ascending part of a ramp depolarization¹³ (Supplementary Fig. 7a). An asymmetric ramp-like depolarization of the baseline membrane potential is therefore a subthreshold signature of place fields.

We next examined the modulation of the amplitude and phase of membrane potential oscillations occurring at theta frequencies during runs along the virtual track. We measured intracellular theta oscillations by band-pass filtering our membrane potential recordings from 6–10 Hz, after action potentials were removed (Fig. 5a and Methods). When the mouse entered the recorded cell's place field, the amplitude

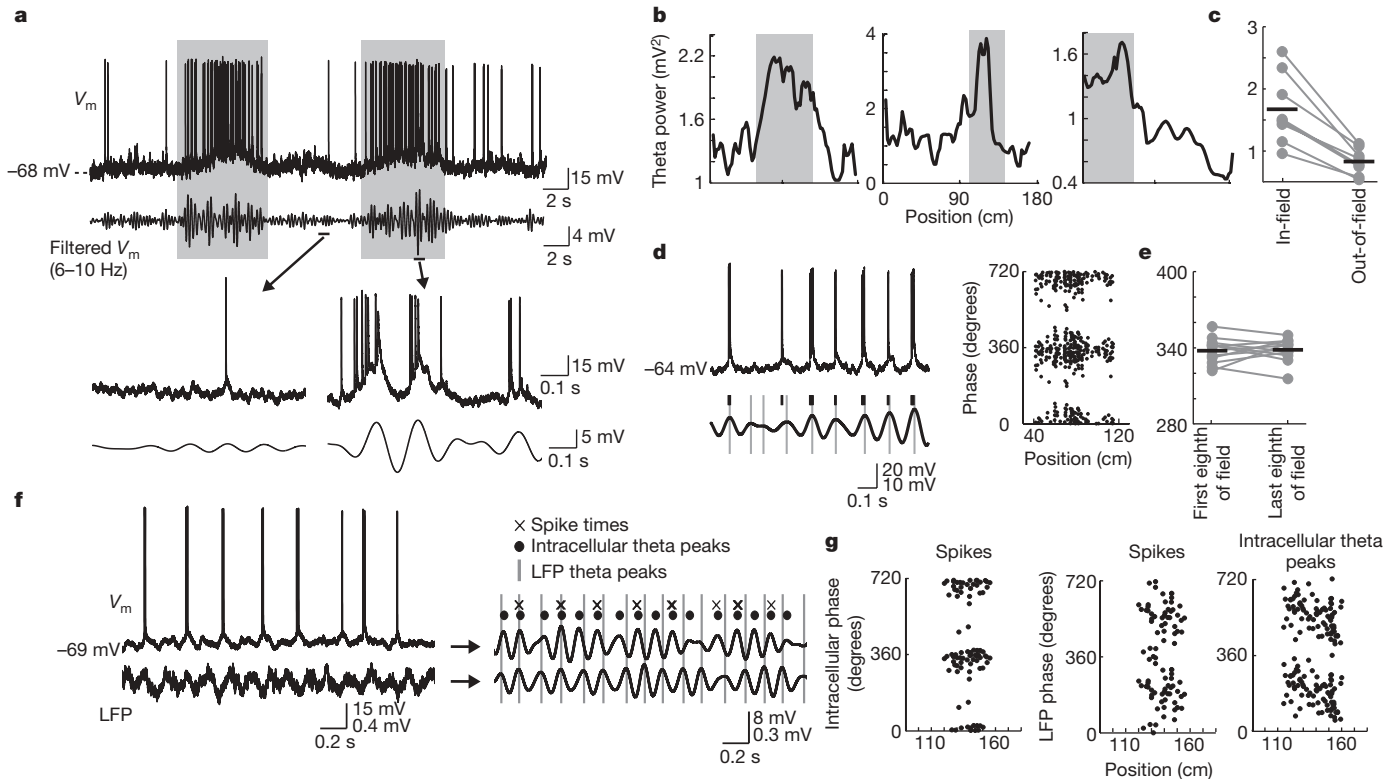


Figure 5 | Membrane potential theta oscillations in place cells. **a**, Top, example raw and filtered (6–10 Hz after spikes were removed) membrane potential traces during runs through the cell's place field (grey boxes). Bottom, expanded portions of the raw and filtered traces. **b**, Power in the theta-frequency band sorted by position along the track for the cells from Fig. 4. Power was measured as the squared amplitude of the filtered trace. Grey boxes denote the primary place fields. **c**, Theta power inside and outside the place field for individual cells. Horizontal bars are means. $n = 8$ cells from 8 mice. **d**, Spike times relative to intracellular theta. Left, example raw and filtered (6–10 Hz) membrane potential traces in the place field. Grey lines indicate peaks of theta oscillations (0°), black lines are times of spikes. Right, example phase (two cycles) versus position plot during place field traversals for a single cell. **e**, Intracellular phase values for spikes in the first and last eighth of the place field for individual place fields. Horizontal lines are the means. $n = 12$ place fields and 8 cells from 8 mice. **f**, Raw (left) and filtered (6–10 Hz, right) membrane potential and LFP traces in the place field from a simultaneous LFP and whole-cell recording. The times of LFP theta peaks (grey lines), intracellular theta peaks (circles) and spikes (crosses) are shown to illustrate the phase precession of spikes and intracellular theta relative to LFP theta oscillations, and the absence of phase precession of spikes relative to intracellular theta oscillations. **g**, Phase precession of spike times relative to intracellular theta (left), relative to LFP theta (middle) and phase precession of intracellular theta peak times relative to LFP theta (right) from a simultaneous LFP and whole-cell recording. In **d** and **f**, the top and bottom scale bar labels denote the top and bottom traces, respectively.

and last eighth of the place field for individual place fields. Horizontal lines are the means. $n = 12$ place fields and 8 cells from 8 mice. **f**, Raw (left) and filtered (6–10 Hz, right) membrane potential and LFP traces in the place field from a simultaneous LFP and whole-cell recording. The times of LFP theta peaks (grey lines), intracellular theta peaks (circles) and spikes (crosses) are shown to illustrate the phase precession of spikes and intracellular theta relative to LFP theta oscillations, and the absence of phase precession of spikes relative to intracellular theta oscillations. **g**, Phase precession of spike times relative to intracellular theta (left), relative to LFP theta (middle) and phase precession of intracellular theta peak times relative to LFP theta (right) from a simultaneous LFP and whole-cell recording. In **d** and **f**, the top and bottom scale bar labels denote the top and bottom traces, respectively.

of intracellular theta oscillations increased (Fig. 5a). Theta-band power in the membrane potential trace was higher in place fields than outside of place fields ($\text{power}_{\text{in-field}} = 1.7 \pm 0.4 \text{ mV}^2$, $\text{power}_{\text{out-of-field}} = 0.8 \pm 0.2 \text{ mV}^2$, $P < 0.01$; Fig. 5b, c and Supplementary Figs 2c and 8). Consistently, theta oscillation amplitude and firing rate were highly correlated ($C = 0.61 \pm 0.09$, $P < 0.001$). In contrast, the amplitude of membrane potential theta oscillations was similar at all spatial locations for putative CA1 pyramidal neurons that did not have a place field (Supplementary Fig. 9) and for the LFP theta rhythm (Supplementary Fig. 10).

To examine the modulation of the phase of intracellular theta, we compared intracellular theta fluctuations with LFP theta oscillations. We began by looking for phase precession of spike times relative to membrane potential theta oscillations. The intracellular phases of spike times did not change during runs through the place field, and the phase and position of spikes were not correlated ($\Delta\text{phase} = 0.6 \pm 10.4^\circ$ between the first and last eighth of the field, $P > 0.9$; $C = -0.01 \pm 0.08$ between phase and position, $P > 0.6$; Fig. 5d–g). Because spike times advanced relative to LFP theta oscillations but not intracellular theta (compare Figs 3d, e and 5d, e), it is predicted that a phase shift between LFP and intracellular theta occurs during place field traversals. We therefore performed simultaneous whole-cell and LFP recordings to compare directly the phases of intracellular and extracellularly recorded theta. During runs through the place field, the phase difference between intracellular and LFP theta shifted such that the intracellular theta oscillation phase precessed relative to the LFP theta rhythm ($C = -0.26 \pm 0.12$ between LFP phase and position for the times of intracellular theta peaks; $n = 2$ cells from 2 mice; Fig. 5f, g and Supplementary Fig. 11a). Consistently, the frequency of intracellular theta oscillations in the place field was higher than the frequency of LFP theta fluctuations (measured as a ratio of periods of intracellular theta to periods of LFP theta; $\text{ratio}_{\text{in-field}} = 0.97 \pm 0.21$, $P < 0.01$ versus 1; $\Delta\text{frequency} = 0.22 \text{ Hz}$ given a mean LFP frequency of 7.4 Hz; see Methods and Supplementary Fig. 11b). In contrast, the frequencies of intracellular theta and LFP theta during epochs outside the place field were similar ($\text{ratio}_{\text{out-of-field}} = 1.01 \pm 0.22$, $P > 0.2$ versus 1; Supplementary Fig. 11b). Intracellular theta oscillations in place cells were therefore not constant in amplitude or phase (relative to LFP theta) throughout runs on the linear track; rather, membrane potential theta oscillations were dynamically modulated across positions in virtual space.

Ramp-like depolarizations of the membrane potential and increases in intracellular theta oscillation amplitude were present simultaneously, which can be demonstrated directly by filtering the membrane potential trace from DC–10 Hz (Fig. 1f). Consistently, intracellular theta power and the baseline membrane potential were highly correlated ($C = 0.52 \pm 0.07$, $P < 0.001$; Figs 4c and 5b and Supplementary Fig. 2b, c). To determine whether ramps of depolarization trigger increases in theta amplitude, we injected ramps of current at the soma while the animal was running along the virtual track, and measured changes in theta power. Theta power increased weakly with higher levels of depolarization; however, the increase in power was smaller than during runs through the place field ($P < 0.01$ at similar ΔV values; compare Figs 4c, 5b and Supplementary Fig. 7b). Ramp-like depolarizations of the membrane potential therefore were not sufficient to cause the increases in theta oscillation amplitude observed in place fields.

Our whole-cell recordings revealed two further subthreshold phenomena. First, in a fraction of our recordings we observed spikelets, brief small amplitude deflections of the membrane potential (2 out of 8 place cells; amplitude = $7.4 \pm 1.3 \text{ mV}$, full-width at half-maximum = $1.6 \pm 0.4 \text{ ms}$; 0.06 ± 0.05 spikelets per second; Supplementary Fig. 12a)³⁵. Second, bursts of action potentials were occasionally followed by large (~ 10 – 25 mV) depolarizations lasting up to 50 – 100 ms ²³ (Supplementary Fig. 12b). These events sometimes contained broadened spikes of reduced amplitude, consistent with Ca^{2+}

spikes recorded in slices³⁶. Further analysis is required to assess the prevalence, significance and mechanisms of these events.

Discussion

Here we have developed a visual virtual-reality system in which head-restrained mice performed spatial behaviours along a virtual linear track. Hippocampal place-cell activities were triggered during runs along the track, with similar properties to those recorded in real environments. Because the mouse was head-restrained, we were able to obtain whole-cell recordings lasting many minutes in awake mice using standard patch-clamp techniques. Furthermore, this set-up can probably be combined with two-photon laser scanning microscopy, which has previously been performed in mice running on the spherical treadmill¹⁹. Virtual reality also offers the ability to design highly custom environments, and to manipulate these environments rapidly through software. We therefore anticipate that our virtual-reality system will make new types of experiments exploring spatial information encoding possible.

We identified three subthreshold signatures of place fields: an asymmetric ramp-like depolarization of the baseline membrane potential, an increase in the amplitude of membrane potential theta oscillations, and a phase precession of intracellular theta relative to LFP theta, such that spike times advanced relative to LFP theta but not intracellular theta (Figs 1f, 4 and 5). These findings seem inconsistent with the mechanisms underlying dual oscillator models^{2,4,14}, network models^{7–9} and an experience-dependent model¹² of hippocampal rate and temporal coding because each model predicts membrane potential dynamics that differ significantly from our observed subthreshold signatures (Figs 1b, c, e–h). Our data are most consistent with a soma-dendritic interference model that proposes interactions between a spatially independent inhibitory oscillatory input near the soma, and a spatially dependent (increasing in the place field) and temporally patterned (at theta) dendritic excitatory input^{10,11,13,15}. With an appropriate choice of conductances¹⁵, the soma-dendritic interference model predicts, in the place field, ramp-like depolarizations (Figs 1d and 4), an increase in theta amplitude (Figs 1d and 5a–c), and precession of intracellular theta relative to extracellular theta (Figs 1i and 5f, g). We note, however, that we observed an asymmetric ramp-like depolarization (Fig. 4e), which may be important for phase precession across the entire place field¹², compared with a symmetric ramp proposed in this model. We do not exclude the possibility that revised forms of other models could potentially explain the intracellular dynamics we observed. Other experiments will be necessary to define and quantify the cellular and synaptic mechanisms underlying the intracellular dynamics we measured, including in the context of the entorhinal cortex^{2,16,37}, and to establish their causal relationship to rate and temporal codes in the hippocampus. The virtual-reality system developed here, combined with electro- and opto-physiological methods, will probably facilitate this analysis.

METHODS SUMMARY

A virtual-reality system was designed using an air-supported spherical treadmill for head-restrained mice¹⁹, in combination with a projection-based visual display system²⁰, in which a toroidal screen presented an image from a projector by an angular amplification mirror²¹. Custom software to control the virtual-reality system was developed on the basis of the Quake2 game engine. Rotations of the spherical treadmill, measured by an optical computer mouse, were used to update the visual display. Water-scheduled C57BL/6J mice (8–12 weeks old) were trained using operant conditioning to run from end-to-end of a virtual linear track (180 cm long) to obtain water rewards. For electrophysiology measurements, a small craniotomy ($\sim 0.5 \text{ mm}$ diameter) was made centred over dorsal hippocampus (2.2 mm caudal, 1.7 mm lateral to bregma). The craniotomy was sealed with silicone grease and then covered with silicone elastomer to allow recordings across several days. Extracellular recordings were made using a glass electrode (filled with 0.5 M NaCl , $\sim 2.5 \text{ M}\Omega$ pipette resistance) mounted on a micromanipulator positioned behind the mouse. Whole-cell recordings were obtained using standard blind patch methods. Patch pipettes were pulled with a long taper ($\sim 100 \mu\text{m}$

diameter at 1 mm from the tip) to minimize damage to the overlying cortical tissue, and were mounted on a micromanipulator positioned outside the field of view. Firing rate maps were calculated for 80 spatial bins along the virtual track as the number of spikes in a bin divided by the time spent in that bin. Changes in baseline membrane potential in the place field were measured from membrane potential traces excluding spikes. Theta oscillations were analysed after band-pass filtering (6–10 Hz) of the membrane potential recording using a linear phase finite impulse response filter.

Full Methods and any associated references are available in the online version of the paper at www.nature.com/nature.

Received 8 July; accepted 15 September 2009.

1. Moser, E. I., Kropff, E. & Moser, M. B. Place cells, grid cells, and the brain's spatial representation system. *Annu. Rev. Neurosci.* **31**, 69–89 (2008).
2. O'Keefe, J. & Burgess, N. Dual phase and rate coding in hippocampal place cells: theoretical significance and relationship to entorhinal grid cells. *Hippocampus* **15**, 853–866 (2005).
3. O'Keefe, J. & Dostrovsky, J. The hippocampus as a spatial map. Preliminary evidence from unit activity in the freely-moving rat. *Brain Res.* **34**, 171–175 (1971).
4. O'Keefe, J. & Recce, M. L. Phase relationship between hippocampal place units and the EEG theta rhythm. *Hippocampus* **3**, 317–330 (1993).
5. Skaggs, W. E., McNaughton, B. L., Wilson, M. A. & Barnes, C. A. Theta phase precession in hippocampal neuronal populations and the compression of temporal sequences. *Hippocampus* **6**, 149–172 (1996).
6. Buzsáki, G. Theta oscillations in the hippocampus. *Neuron* **33**, 325–340 (2002).
7. Tsodyks, M. V., Skaggs, W. E., Sejnowski, T. J. & McNaughton, B. L. Population dynamics and theta rhythm phase precession of hippocampal place cell firing: a spiking neuron model. *Hippocampus* **6**, 271–280 (1996).
8. Jensen, O. & Lisman, J. E. Hippocampal CA3 region predicts memory sequences: accounting for the phase precession of place cells. *Learn. Mem.* **3**, 279–287 (1996).
9. Wallenstein, G. V. & Hasselmo, M. E. GABAergic modulation of hippocampal population activity: sequence learning, place field development, and the phase precession effect. *J. Neurophysiol.* **78**, 393–408 (1997).
10. Kamondi, A., Acsady, L., Wang, X. J. & Buzsaki, G. Theta oscillations in somata and dendrites of hippocampal pyramidal cells *in vivo*: activity-dependent phase-precession of action potentials. *Hippocampus* **8**, 244–261 (1998).
11. Magee, J. C. Dendritic mechanisms of phase precession in hippocampal CA1 pyramidal neurons. *J. Neurophysiol.* **86**, 528–532 (2001).
12. Mehta, M. R., Lee, A. K. & Wilson, M. A. Role of experience and oscillations in transforming a rate code into a temporal code. *Nature* **417**, 741–746 (2002).
13. Harris, K. D. *et al.* Spike train dynamics predicts theta-related phase precession in hippocampal pyramidal cells. *Nature* **417**, 738–741 (2002).
14. Lengyel, M., Szatmary, Z. & Erdi, P. Dynamically detuned oscillations account for the coupled rate and temporal code of place cell firing. *Hippocampus* **13**, 700–714 (2003).
15. Gasparini, S. & Magee, J. C. State-dependent dendritic computation in hippocampal CA1 pyramidal neurons. *J. Neurosci.* **26**, 2088–2100 (2006).
16. Maurer, A. P. & McNaughton, B. L. Network and intrinsic cellular mechanisms underlying theta phase precession of hippocampal neurons. *Trends Neurosci.* **30**, 325–333 (2007).
17. Lee, A. K., Manns, I. D., Sakmann, B. & Brecht, M. Whole-cell recordings in freely moving rats. *Neuron* **51**, 399–407 (2006).
18. Lee, A. K., Epszttein, J. & Brecht, M. Head-anchored whole-cell recordings in freely moving rats. *Nature Protocols* **4**, 385–392 (2009).
19. Dombeck, D. A., Khabbaz, A. N., Collman, F., Adelman, T. L. & Tank, D. W. Imaging large-scale neural activity with cellular resolution in awake, mobile mice. *Neuron* **56**, 43–57 (2007).
20. Hölscher, C., Schnee, A., Dahmen, H., Setia, L. & Mallot, H. A. Rats are able to navigate in virtual environments. *J. Exp. Biol.* **208**, 561–569 (2005).
21. Chahl, J. S. & Srinivasan, M. V. Reflective surfaces for panoramic imaging. *Appl. Opt.* **36**, 8275–8285 (1997).
22. Ranck, J. B. Jr. Studies on single neurons in dorsal hippocampal formation and septum in unrestrained rats. I. Behavioral correlates and firing repertoires. *Exp. Neurol.* **41**, 461–531 (1973).
23. Kandel, E. R. & Spencer, W. A. Electrophysiology of hippocampal neurons. II. After-potentials and repetitive firing. *J. Neurophysiol.* **24**, 243–259 (1961).
24. Quirk, M. C. & Wilson, M. A. Interaction between spike waveform classification and temporal sequence detection. *J. Neurosci. Methods* **94**, 41–52 (1999).
25. McNaughton, B. L., Barnes, C. A. & O'Keefe, J. The contributions of position, direction, and velocity to single unit activity in the hippocampus of freely-moving rats. *Exp. Brain Res.* **52**, 41–49 (1983).
26. Nakazawa, K. *et al.* Hippocampal CA3 NMDA receptors are crucial for memory acquisition of one-time experience. *Neuron* **38**, 305–315 (2003).
27. Kentros, C. G., Agnihotri, N. T., Streeter, S., Hawkins, R. D. & Kandel, E. R. Increased attention to spatial context increases both place field stability and spatial memory. *Neuron* **42**, 283–295 (2004).
28. Cacucci, F., Wills, T. J., Lever, C., Giese, K. P. & O'Keefe, J. Experience-dependent increase in CA1 place cell spatial information, but not spatial reproducibility, is dependent on the autophosphorylation of the alpha-isoform of the calcium/calmodulin-dependent protein kinase II. *J. Neurosci.* **27**, 7854–7859 (2007).
29. Sun, L. D. & Wilson, M. A. *Impaired and Enhanced Spatial Representations of the PSD-95 Knockout Mouse*. PhD thesis, Massachusetts Institute of Technology (2003).
30. Margrie, T. W., Brecht, M. & Sakmann, B. *In vivo*, low-resistance, whole-cell recordings from neurons in the anaesthetized and awake mammalian brain. *Pflugers Arch.* **444**, 491–498 (2002).
31. Crochet, S. & Petersen, C. C. Correlating whisker behavior with membrane potential in barrel cortex of awake mice. *Nature Neurosci.* **9**, 608–610 (2006).
32. Wilson, M. A. & McNaughton, B. L. Dynamics of the hippocampal ensemble code for space. *Science* **261**, 1055–1058 (1993).
33. Guzowski, J. F., McNaughton, B. L., Barnes, C. A. & Worley, P. F. Environment-specific expression of the immediate-early gene Arc in hippocampal neuronal ensembles. *Nature Neurosci.* **2**, 1120–1124 (1999).
34. Henze, D. A. *et al.* Intracellular features predicted by extracellular recordings in the hippocampus *in vivo*. *J. Neurophysiol.* **84**, 390–400 (2000).
35. Kandel, E. R. & Spencer, W. A. Electrophysiology of hippocampal neurons. IV. Fast prepotentials. *J. Neurophysiol.* **24**, 272–285 (1961).
36. Wong, R. K. & Prince, D. A. Participation of calcium spikes during intrinsic burst firing in hippocampal neurons. *Brain Res.* **159**, 385–390 (1978).
37. Hafting, T., Fyhn, M., Bonnevie, T., Moser, M. B. & Moser, E. I. Hippocampus-independent phase precession in entorhinal grid cells. *Nature* **453**, 1248–1252 (2008).

Supplementary Information is linked to the online version of the paper at www.nature.com/nature.

Acknowledgements We thank E. Chaffin for help with mouse behaviour, J. Carmack and id Software for providing the Quake2 code, A. Shishlov for programming advice, G. Buzsaki, J. Magee, H. Dahmen and D. Markowitz for discussions, and C. Brody, M. Berry and E. Civillico for comments on the manuscript. This work was supported by the NIH (1R01MH083686-01, 5R01MH060651-09), a Helen Hay Whitney Fellowship (to C.D.H.), and a Patterson Trust Fellowship (to D.A.D.).

Author Contributions C.D.H. performed behaviour and intracellular recording experiments with technical assistance from D.A.D. C.D.H. and D.A.D. performed extracellular recording experiments. F.C., D.A.D. and D.W.T. designed, and C.D.H., F.C. and D.W.T. implemented, the virtual-reality instrumentation. F.C. performed virtual-reality software development. C.D.H. analysed all data with strategy and methods contributions from all authors. C.D.H. and D.W.T. wrote the paper.

Author Information Reprints and permissions information is available at www.nature.com/reprints. Correspondence and requests for materials should be addressed to D.W.T. (dwtank@princeton.edu).

METHODS

Virtual-reality set-up. The virtual-reality system (Fig. 2a and Supplementary Fig. 1) was designed around an air-supported spherical treadmill (8-inch diameter Styrofoam ball) for head-restrained mice that was previously used for *in vivo* optical imaging at cellular resolution¹⁹. A projection-based visual display, similar to the system used in a body-tethered rat virtual-reality system²⁰, presented a computer rendered scene with a 270° horizontal field of view and a vertical field from +60° to -20° relative to the mouse's head. The toroidal screen displayed the two-dimensional image from a Mitsubishi HC3000 digital light processing projector reflected off of a 15 cm diameter round mirror and a 15 cm diameter angular amplification mirror (AAM)²¹ with an angular amplification factor of 12. The AAM was machined out of aluminium using a CNC machine and then polished by hand. The screen was ~46 cm tall and ~80 cm in outer diameter, and was constructed out of a semi-reflective nylon material (Rose Brand fabrics) supported by a frame of stainless steel rods. Water rewards were delivered by a solenoid valve (NResearch) attached to a water-feeding tube (Popper and Sons) positioned directly in front of the animal's mouth such that the mouse could lick the meniscus. Rotations of the Styrofoam ball were measured by an optical computer mouse (Logitech MX1000) that was positioned below the field of view in front of the animal at the point where the ball's equator intersected the animal's rostral-caudal body axis. A computer running Labview used USB-communicated signals from the optical mouse to compute low-pass filtered ball rotational velocity around both the horizontal axis (perpendicular to the body axis) and vertical axis. These velocities were then output as analogue control voltages using a D/A converter (National Instruments) and used as input control signals to a separate computer running the virtual-reality software.

The virtual-reality software we developed was on the basis of the open source Quake2 game engine (id software), using code ported to Visual Studio 2008 (Microsoft). The rendering engine was modified, using cube map texturing in OpenGL graphics³⁸, to display a 'fisheye' transform of the perspective of the virtual player, such that the image reflected off the AAM and displayed on the screen had the geometrically correct perspective for the mouse on the ball. Software to control the water reward system, input information on ball rotation velocity, and output voltages proportional to position and view angle within the environment was also developed by adding A/D and D/A control to the game engine, using National Instruments multifunction cards. Ball velocity around the vertical axis was used as a control signal for changing view angle in the virtual environment, whereas velocity around the horizontal axis was used as a control signal for forward and backward movement. Other open source gaming software (Quark, <http://quark.planetquake.gamespy.com/>) was used to build the virtual linear track. To synchronize behaviour data with electrophysiology recordings, an independent computer with a Digidata 1440A interface running Clampex software (Molecular Devices) digitized and stored real time information about the mouse's location in the virtual environment together with solenoid (water reward) control signals, ball rotational velocities, and electrophysiological data. **Behavioural training.** Eight-to-twelve-week-old male C57BL/6J mice (Jackson Labs) were used for all experiments. C57BL/6J mice were selected because they have good vision compared to other inbred strains³⁹ and are a common background strain for transgenic mice. All experimental procedures were performed in compliance with the Guide for the Care and Use of Laboratory Animals (<http://www.nap.edu/readingroom/books/labrats/>) and were approved by Princeton University's Institutional Animal Care and Use Committee. Before behavioural training, titanium head plates with a large central opening (2.5 cm wide × 0.9 cm long × 0.08 cm thick; central opening: 0.89 cm wide × 0.61 cm long) were implanted on mice and affixed to the skull using dental cement (Metabond, Parkell). Sites for future craniotomies over the left and right dorsal hippocampi were marked using stereotactic coordinates (2.2 mm caudal, 1.7 mm lateral to bregma). After head plate implantation, mice were placed on a water schedule in which they received 1 ml of water per day. Body weights were checked to ensure mice were ~80% of their pre-water-restriction weight^{40,41}.

After at least 5 days of water scheduling, behaviour training began. In each training session, mice were placed on the experimental apparatus with their head fixed in place. The head was centred over the middle of the Styrofoam ball with the headplate ~2.6 cm from the top of the ball. A lick tube to deliver water rewards was positioned in front of the mouse's mouth. The water rewards earned during behaviour were included in the mouse's daily water allotment such that a mouse received exactly 1 ml of water per day. Each training session (one per day) lasted 45 min with the virtual-reality system turned on for all sessions. The first several sessions mostly involved acclimation to the apparatus and learning to run on the spherical treadmill.

Mice were trained to perform behaviours along a virtual linear track. The virtual track was 180 cm long and 9 cm wide, measured as the number of rotations

of the Styrofoam ball to move from one end of the track to the other times the circumference of the ball. The effective width of the track (that is, the distance the mouse could actually move) was ~1 cm, rather than 9 cm, because in Quake2 the player is surrounded by a bounding box that gives him a fixed width. The track had short proximal walls with different textures for each third of the track (0–60 cm: white with black dots, 61–120 cm: vertical white and black stripes, 121–180 cm: black with white dots). The proximal walls at the ends of the track were green with black dots to mark the reward zones. Tall distal walls were positioned at 60 cm (horizontal black and white stripes) and 120 cm (green with black crosses). The floor and ceiling were black throughout the track. Green was selected as the only non-black or white colour because electrophysiological and behavioural data indicate that mice can detect wavelengths of ~500 nm⁴². Mice received small water rewards (4 µl) for running between reward zones positioned at opposite ends of the track (zone 1 position: 0–9 cm; zone 2 position: 171–180 cm). After receiving a reward at one reward zone, the mouse then had to run to the other reward zone to receive the next reward; two consecutive rewards could not be obtained from a single reward site. Linear track behavioural data (Fig. 2c–e) were from mice trained only on the linear track. Some animals used for electrophysiology recordings were trained in other virtual environments before training in the linear track. During electrophysiology experiments, behavioural performance was in some cases degraded due to satiation from water rewards and because the visual display was turned off while patch pipettes were changed.

Electrophysiology. After at least five training sessions on the virtual linear track, a small craniotomy (~0.5 mm diameter) was made over the left hippocampus (2.2 mm caudal, -1.7 mm lateral to bregma). The dura was left intact for both extracellular and intracellular recordings. Because behavioural performance was degraded on the day of surgery and anaesthesia, electrophysiology recordings were performed starting the next day. To preserve the craniotomy across days, it was covered with silicone grease (Dow Corning) and then with a layer of silicone elastomer (Kwik-Sil, World Precision Instruments) until the time of recording. Extracellular recordings (Fig. 3 and Supplementary Fig. 10) were made using a single glass electrode filled with 0.5 M NaCl (~2.5 MΩ pipette resistance). The electrode was mounted vertically (perpendicular to the surface of the brain) on a micromanipulator (Sutter MP285) that was positioned behind the mouse and thus outside the mouse's field of view. The reference electrode was positioned outside the craniotomy in extracellular saline containing (in mM): 150 NaCl, 2.5 KCl, 10 HEPES, pH 7.4. Signals were electronically filtered between 500 Hz and 7.5 kHz and digitized at 20 kHz. For measurements of the LFP and phase precession, signals were electronically filtered between 2 Hz and 10 kHz; spikes and the LFP were recorded on the same electrode. The position of the top of the brain was noted as a large resistance increase when the electrode made contact with the dura. As the electrode was advanced through cortex, spikes were present in each layer. Upon entering the external capsule, a change in the recording was noted, especially from changes in sound quality using an audio monitor. The CA1 cell body layer was ~200 µm beneath the external capsule and was characterized by strongly theta-modulated spiking. Putative pyramidal neurons were found as units firing complex bursts separated at theta frequencies²². In all animals CA1 recordings were made at a depth of ~1.1 mm; cells were found reproducibly at this depth across several electrodes and days. To confirm that this recording position was in the CA1 cell body layer, in a separate experiment we electroporated Alexa 488 dextran (5% (w/v) in extracellular saline, 4 µA pulses, 25 ms pulse duration, 600 pulses at 2 Hz) using a recording pipette and found bright labelling of CA1 cell bodies in histology sections. At this depth, we searched for well-isolated units of large amplitude and recorded their activity for ~15–30 min, which was enough time for the mouse to sample thoroughly the virtual linear track. Spikes were sorted offline using a threshold analysis. At most one unit was isolated from a single recording. To check the quality of unit isolation, we overlaid all spike waveforms to make sure that they matched by visual inspection (Fig. 3a), and we plotted ISI distributions to make sure no spikes fell within the refractory period (<1–2 ms; Fig. 3b). Extracellular recordings were made from a total of 8 mice. In some cases a second craniotomy was made over the right hemisphere to extend the number of recording sessions from a single animal. Recordings were made for up to 4 days from the same craniotomy. Place cells were found in every mouse tested.

Whole-cell recordings were made using the same experimental set-up as for extracellular recordings. Pipettes (~5–7 MΩ) were filled with internal solution containing (in mM): 135 K-gluconate, 10 HEPES, 10 Na₂-phosphocreatine, 4 KCl, 4 MgATP, 0.3 Na₃GTP (pH 7.25 with KOH, 285 mOsm). We pulled pipettes with a long taper (~100 µm diameter at 1 mm from the tip) to minimize damage to the overlying cortical tissue and to reduce compression of the tissue while advancing the pipette. The pipette was mounted vertically on a standard micromanipulator (Sutter MP285) positioned outside the mouse's field of view; special methods to anchor the pipette^{17,18} were not necessary. We used standard blind patch methods to obtain whole-cell recordings³⁰. In brief, we applied ~250 mbar of positive pressure

while moving the pipette through the cortex and reduced the pressure to ~ 15 mbar while searching for cells in the hippocampus. The CA1 cell body layer was located using a depth coordinate obtained from extracellular recordings in the same animal. We attempted to form a seal when we observed large ($\sim 50\%$), reproducible increases in pipette resistance. Recordings were made in current clamp mode with no holding current. Membrane potential values were corrected for liquid junction potentials. We obtained recordings lasting longer than 3 min from 46 cells from 15 mice, with a peak success rate of approximately one such recording in every five attempts. Recordings were abandoned when we observed large increases in resting potential or large decreases in spike amplitude. We obtained whole-cell recordings for up to 3 days from the same craniotomy. Whole-cell recordings from place cells lasted on average 7.1 ± 2.8 min and had series resistances of 48 ± 16 M Ω , input resistances of 98 ± 23 M Ω , and resting membrane potentials of -67 ± 4 mV. Firing rates from place cells recorded intracellularly tended to be higher than those recorded extracellularly, both inside and outside the place field, potentially because a fraction of spikes measured extracellularly were lost during spike sorting. All other place-cell parameters (for example, field size, ISI distribution) were similar between cells recorded extracellularly and intracellularly. Although we cannot exclude possible effects of dialysis of the cell during whole-cell measurements, such effects are probably small owing to short recording durations and relatively high series resistances. In experiments to assess the connection between ramps of depolarization and changes in theta oscillation amplitude (Supplementary Fig. 7), ramps of current (4 s duration, 1–1.5 nA at the peak) were injected at the soma after 11 s without current injection. Only trials in which the animal was running at greater than 10 cm s^{-1} were analysed.

To perform whole-cell and extracellular recordings simultaneously (Fig. 5f, g and Supplementary Fig. 11), we mounted two glass electrodes on separate micro-manipulators, which were both positioned behind the mouse, and advanced the electrodes independently through separate craniotomies on the same hemisphere. Whole-cell recordings were made at the standard coordinates as described earlier. The extracellular recording electrode (filled with 0.5 M NaCl) was mounted at a 40° angle relative to the midline and a 45° angle with respect to the vertical. The craniotomy for the extracellular electrode was positioned caudal and either lateral for the left hemisphere or medial for the right hemisphere relative to the craniotomy for intracellular recordings. The tip of the extracellular electrode was positioned at a depth of ~ 1.2 mm and $\sim 250 \mu\text{m}$ caudal to the centre of the craniotomy for whole-cell recordings. The extracellular recordings were filtered between 1 Hz and 10 kHz.

From our 46 hippocampal whole-cell recordings, 41 cells were spontaneously active (overall firing rate > 0.05 Hz). We classified 7 of the spontaneously active cells as interneurons on the basis of high overall firing rates (> 5 Hz) and the absence of complex spike bursts. The remaining 34 spontaneously active cells were categorized as pyramidal neurons. To estimate the fraction of spontaneously active pyramidal neurons that had a place field along the virtual linear track, we considered only those recordings during which the animal visited each of the 80 spatial segments at least 3 times, with visits separated by at least 2 s in time. We estimate that 36% of spontaneously active pyramidal neurons had place fields in the virtual environment (8 out of 22 cells). During whole-cell place-cell recordings, the place field was visited 20 ± 8 times on average, with visits separated by at least 2 s in time.

Data analysis. To create firing rate maps (Figs 3c, 4b and Supplementary Fig. 2a), we divided the virtual linear track into 80 bins (2.25 cm each) and calculated the firing rate as the total number of spikes in a bin divided by the total amount of time spent in a bin. The maps were smoothed using a five point Gaussian window with a standard deviation of one. Periods in which the mouse ran slower than 5 cm s^{-1} , averaged over a 2-s window, were removed from the analysis. To identify place fields, we found groups of adjacent bins with firing rates greater than 0.25 times the rate in the peak bin. We selected only those fields that were larger than 8 bins (18 cm) in length, had mean in-field firing rates of greater than 1.5 Hz, and had mean in-field firing rates more than 3 times larger than the mean out-of-field firing rate. To verify that place fields were a statistically significant increase in firing rate, we performed a bootstrap shuffle test. We shuffled the times of spikes in 10 s segments, calculated new firing rate maps using the unshuffled bin dwell times, and then checked for a place field using the above-stated criteria. This procedure was repeated 1,000 times per place-cell recording. We called a cell a place cell only if a place field was found in the unshuffled data and in fewer than 2% of the shuffled tests ($P < 0.02$). Across the place cells we recorded, we found place fields at all positions along the linear track. Spikes were separated into leftward and rightward runs based on the head direction of the animal with regard to the virtual track (measured as the player's view angle in Quake2). A directionality index for firing based on firing rates in leftward and rightward directions ($FR_{\text{left}}, FR_{\text{right}}$) was defined as $|FR_{\text{left}} - FR_{\text{right}}| / (FR_{\text{left}} + FR_{\text{right}})$. A directionality index of 0 indicates identical firing in both directions, whereas an index of 1 indicates firing in one direction only.

To quantify the average baseline membrane potential as a function of position along the virtual track (Fig. 4c and Supplementary Fig. 2b), we first removed the contribution of action potentials by discarding all time points between 4 ms before and 7 ms after an action potential's peak. We then created a map of membrane potential values by grouping the membrane potentials into 80 spatial bins along the track and calculating an average membrane potential for each bin. The membrane potential map was smoothed using a five point Gaussian window with a standard deviation of one. Large, long-lasting depolarizations of the baseline membrane potential occurred infrequently outside the place field (2.3 ± 1.3 events per recording for depolarizations of greater than 2 mV lasting longer than 0.5 s).

To analyse ramps of depolarization during complete runs through the place field (that is, the mouse did not turn around inside the place field), we calculated changes in membrane potential (ΔV) after action potentials were removed (Fig. 4e and Supplementary Figs 5 and 6b). We defined the baseline membrane potential as the mean membrane potential from 500 ms to 1 s before the mouse entered the place field and subtracted this baseline from all membrane potential values during the run to get ΔV values. The peak ΔV during a run through the place field (Supplementary Fig. 6b) was calculated after smoothing the ΔV values over a sliding window of length 50 ms such that the peak value was representative of the ramp-like depolarization rather than brief, high frequency depolarizations. To analyse the symmetry of firing rates and ramps of depolarization in place fields (Fig. 4e), we considered runs starting half the place field's width before the place field and ending half the place field's width beyond the place field (total length was twice the length of the place field). Because place fields varied in size between cells and runs through the field differed in duration, we divided each run into 60 equally sized spatial bins and calculated the mean firing rates and ΔV for each 1/60th of the run (that is, 15 spatial bins before the place field, 30 bins in the field, and 15 bins after the field). All runs through the field were plotted with increasing track position values so that runs in opposite directions could be combined.

To analyse subthreshold theta oscillations (Fig. 5 and Supplementary Figs 2c, 7 and 9), spikes were removed over a window of 3 ms preceding and 5 ms after the peak and were replaced using linear interpolation. The resulting trace was then band-pass filtered between 6–10 Hz (a peak in the ISI distribution) using a linear phase finite impulse response (FIR) filter with a Hamming window of width 1 s (Matlab function fir1). To create a map of theta power along the virtual track, power was calculated as the mean of the squared amplitude for a sliding window of length 1 s for the entire recording, with the centre of the window providing the position along the track. The power values were grouped into 80 spatial bins along the track and smoothed using a five point Gaussian window with a standard deviation of one. Power spectra for epochs in and out of the place field were obtained using multi-taper spectral analysis methods (Chronux toolbox, <http://chronux.org>; Supplementary Fig. 8). Running speed, which can influence theta oscillations⁴³, was similar inside and outside the place field (in-field speed = $49 \pm 6 \text{ cm s}^{-1}$, out-of-field speed = $47 \pm 4 \text{ cm s}^{-1}$, $P > 0.7$). LFP theta oscillations were present when the animal was running (Fig. 3d and Supplementary Fig. 10) and absent when the animal was resting.

To analyse phase precession (Figs 3d, e and 5d–g), we considered complete runs through the place field (that is, the animal did not turn around in the field) that had at least 5 spikes and in which the animal ran faster than 10 cm s^{-1} . Only cells with more than 40 total spikes in the place field were included. Extracellular or intracellular (after removing spikes) voltage traces were band-pass filtered between 6–10 Hz using an FIR filter. To assign a phase to a spike occurring at time t , we identified, in the filtered trace, the times of the peaks immediately preceding and following the spike (t_1 and t_2 , respectively) and calculated the phase as $360(t - t_1)/(t_2 - t_1)$. We circularly shifted the phase of the spikes in 1° steps from 0° to 360° , continuing across the 360° border, and fit a linear regression line to the phase versus position plot at each rotation⁴³. We found the rotation with the best fit, such that the sum of squared errors between the fit line and data was minimized, and used the correlation coefficient between phase and position at this rotation as a measure of phase precession. All phase values are from the raw data in relation to theta phase, with 0° indicating the peak. To measure the precession of intracellular theta relative to extracellular theta (Fig. 5g), we first identified the times of the peaks of the filtered (6–10 Hz) membrane potential trace during runs through the place field. For each peak of intracellular theta, we found the corresponding phase of the simultaneously recorded extracellular theta and the position of the mouse along the virtual track and followed the same procedures that were used for the analysis of the phase precession of spike times. To quantify the change in times between intracellular theta peaks and LFP theta peaks during place field traversals (Supplementary Fig. 11a), we found the time difference between the first LFP theta peak and the first intracellular theta peak in the place field, the time difference between the second LFP theta peak and the second intracellular theta peak, and so on. To quantify frequency differences between intracellular and LFP theta (Supplementary Fig. 11b), we calculated the ratio of the period of the first intracellular oscillation to the period of the first LFP oscillation, the ratio of the period of

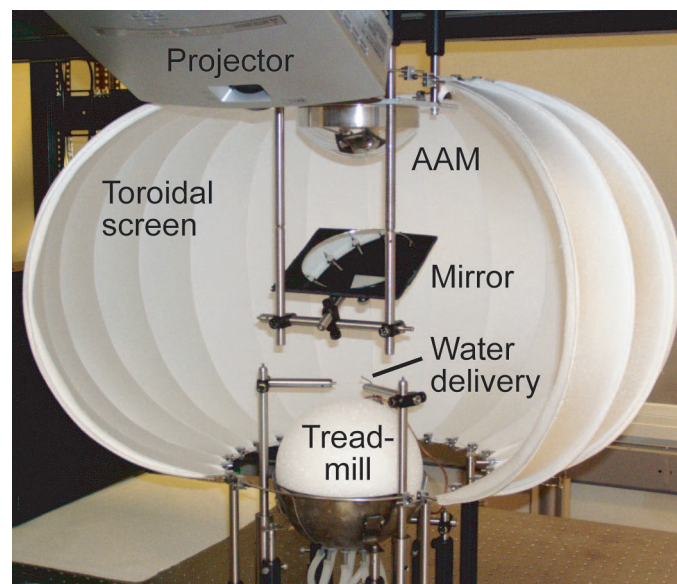
the second intracellular oscillation to the period the second LFP oscillation, and so on using peaks from the filtered (6–10 Hz) traces. We determined these ratios for complete runs through the place field and 3 s long epochs outside the place field.

Data are presented as mean \pm s.d. unless noted otherwise. P values are from two-tailed t -tests unless stated otherwise. Correlation coefficients (C) are from Pearson's correlations.

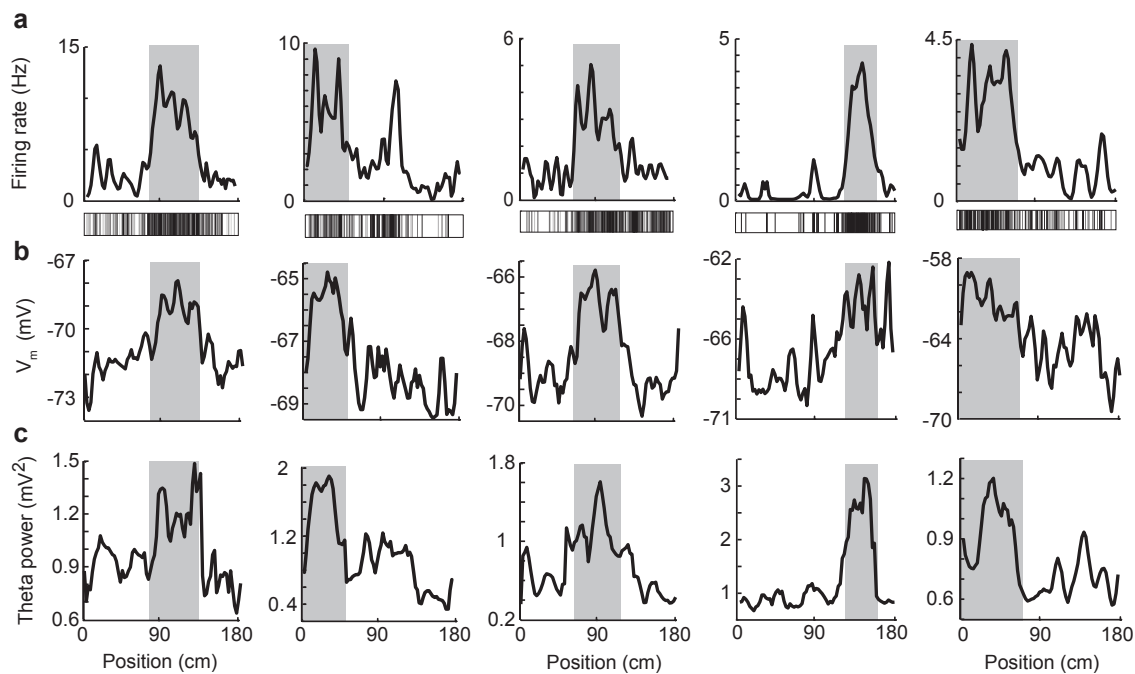
38. Greene, N. Environment mapping and other applications of world projections. *IEEE Comput. Graph. Appl.* **6**, 21–29 (1986).

39. Wong, A. A. & Brown, R. E. Visual detection, pattern discrimination and visual acuity in 14 strains of mice. *Genes Brain Behav.* **5**, 389–403 (2006).
40. Rinberg, D., Koulakov, A. & Gelperin, A. Sparse odor coding in awake behaving mice. *J. Neurosci.* **26**, 8857–8865 (2006).
41. Huber, D. *et al.* Sparse optical microstimulation in barrel cortex drives learned behaviour in freely moving mice. *Nature* **451**, 61–64 (2008).
42. Jacobs, G. H., Neitz, J. & Deegan, J. F. II. Retinal receptors in rodents maximally sensitive to ultraviolet light. *Nature* **353**, 655–656 (1991).
43. Buzsáki, G., Leung, L. W. & Vanderwolf, C. H. Cellular bases of hippocampal EEG in the behaving rat. *Brain Res.* **287**, 139–171 (1983).

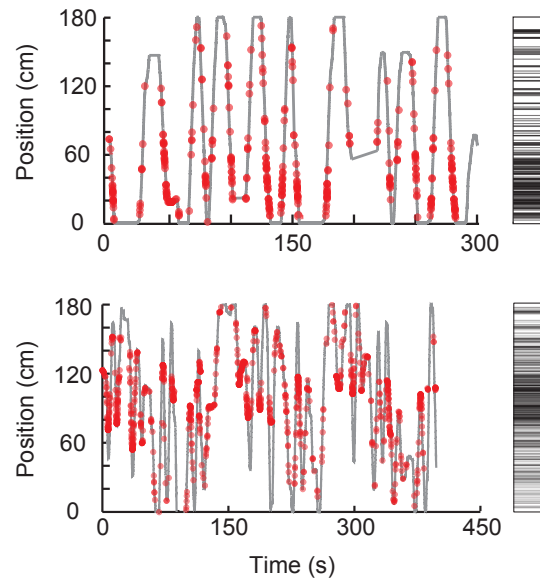
SUPPLEMENTARY INFORMATION



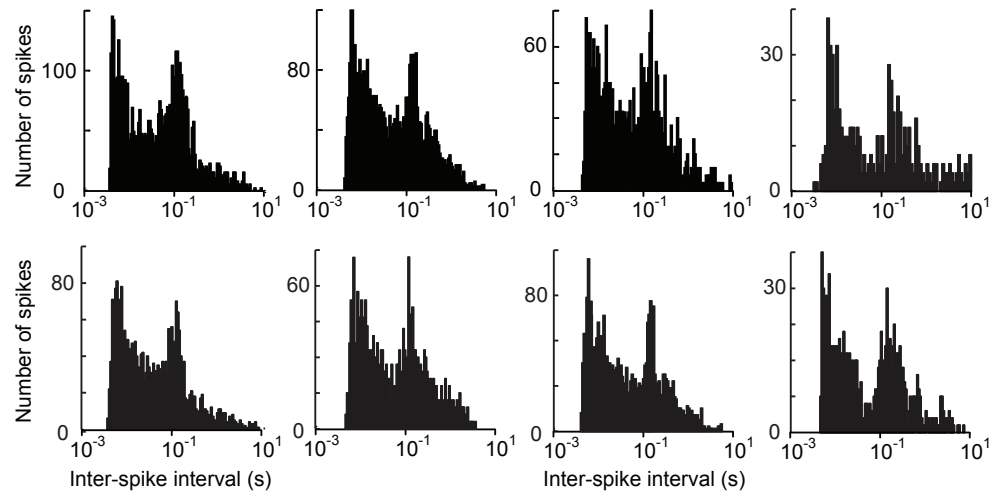
Supplementary Figure 1 | Photograph of the virtual reality setup. A head-restrained mouse runs on an air-supported spherical treadmill. An image from a projector is projected onto a toroidal screen via a reflecting mirror and an angular amplification mirror (AAM). Water rewards are delivered through a lick tube. Electrophysiology setup is not shown. See Methods and Fig. 2A for details.



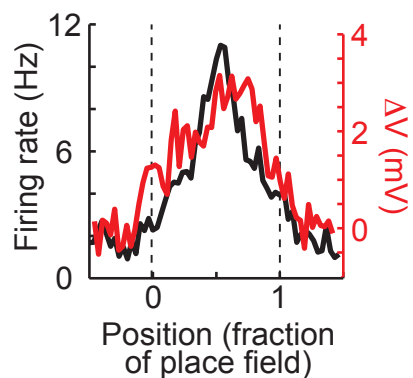
Supplementary Figure 2 | Firing rates, membrane potential depolarizations, and theta power for five place cells recorded intracellularly. **a**, Firing rates along the virtual linear track for 5 place cells from 5 different animals. The gray boxes indicate the primary place field determined by firing rates. Bottom, vertical lines mark the location along the track of every action potential in the recording. These cells are different than those shown in Figs. 4, 5. **b**, Average baseline membrane potential, excluding action potentials, sorted by position along the track for the five place cells from (a). **c**, Power in the theta-frequency band sorted by position along the track for the whole cell recordings from (a). Power was measured as the squared amplitude of the band-pass (6–10 Hz) filtered membrane potential trace.



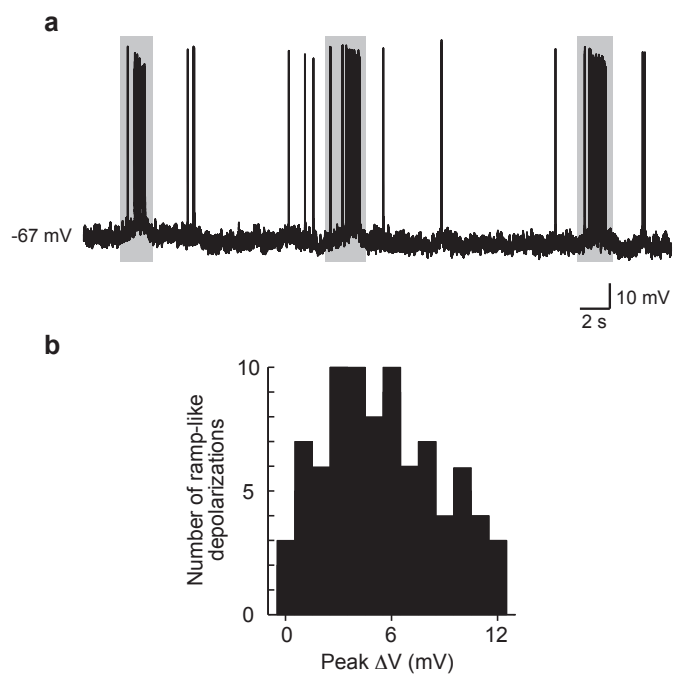
Supplementary Figure 3 | Trajectories and spike positions for two example place cells recorded intracellularly. Left, the position of the animal along the virtual track is shown as a function of time (gray). Red dots indicate the position and time of each spike in the recording. The dots are semi-transparent to illustrate overlapping dots. Right, the position along the track for all spikes from the recording are shown as horizontal lines.



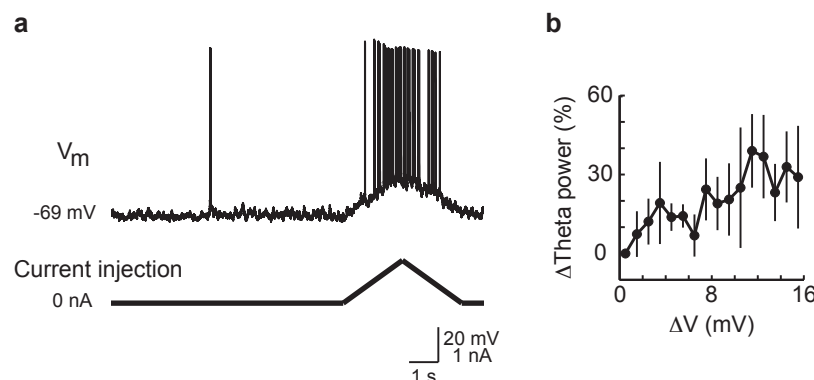
Supplementary Figure 4 | Inter-spike interval distributions from place cells recorded intracellularly. The time axis is plotted on a log scale.



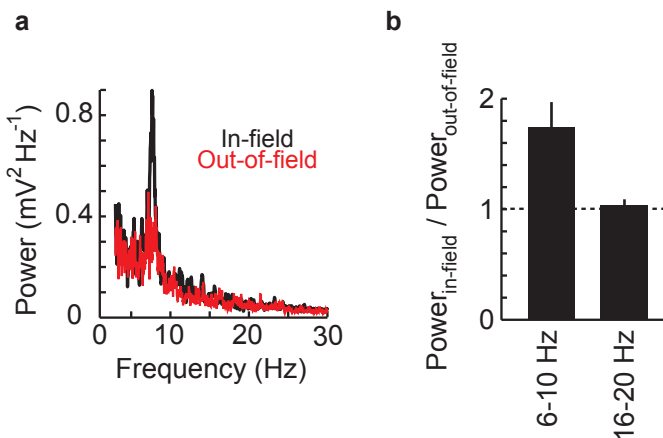
Supplementary Figure 5 | Firing rates (black) and membrane potential depolarization (red) for direct runs through the place field. Data are taken from Fig. 4e. To compare across cells, the position values in the place field were normalized. The values are averaged over 8 cells, including 84 complete runs through the place field.



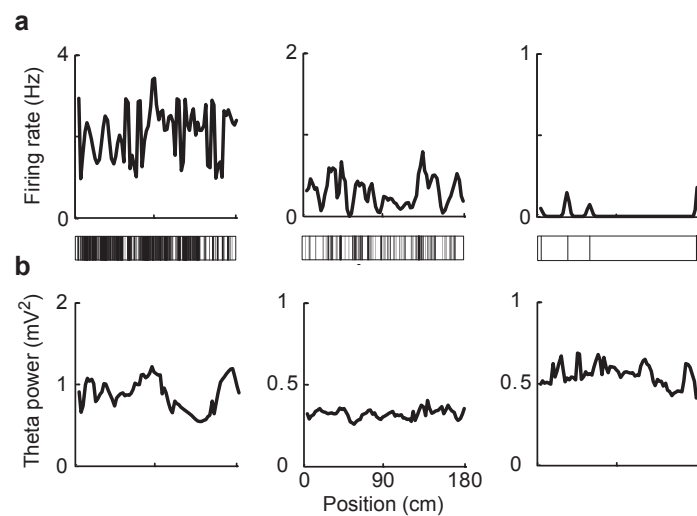
Supplementary Figure 6 | Ramp-like depolarizations during place field traversals. **a**, Example membrane potential trace. Gray boxes indicate the place field. **b**, Histogram of peak membrane potential changes (ΔV), excluding action potentials, during complete runs through the place field. Data are from 84 runs from 8 cells.



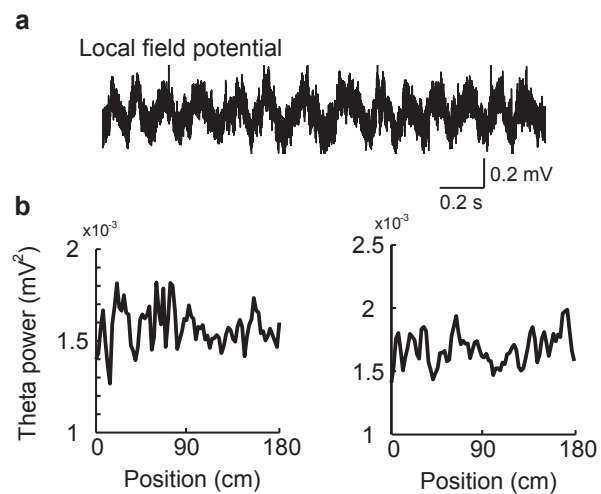
Supplementary Figure 7 | Membrane potential theta oscillations during ramps of depolarization induced by current injections. **a**, Example membrane potential trace. Ramps of current were injected (4 s duration, 1-1.5 nA peak) following 11 seconds without any current injection. **b**, Changes in theta power as a function of depolarization level. ΔV is the membrane potential at a given point minus the mean baseline membrane potential. ΔV values were grouped into 1 mV bins; the value is plotted at the center of the bin. Theta power was measured as the squared amplitude of the membrane potential trace filtered between 6-10 Hz. ΔTheta power was calculated as the theta power minus the theta power in the $0 < \Delta V < 1$ mV bin and plotted as percentage. Error bars indicate mean \pm sem. $n = 6$ putative pyramidal cells and 1 place cell from 3 mice. Data were consistent between the place cell and the non-place cells.



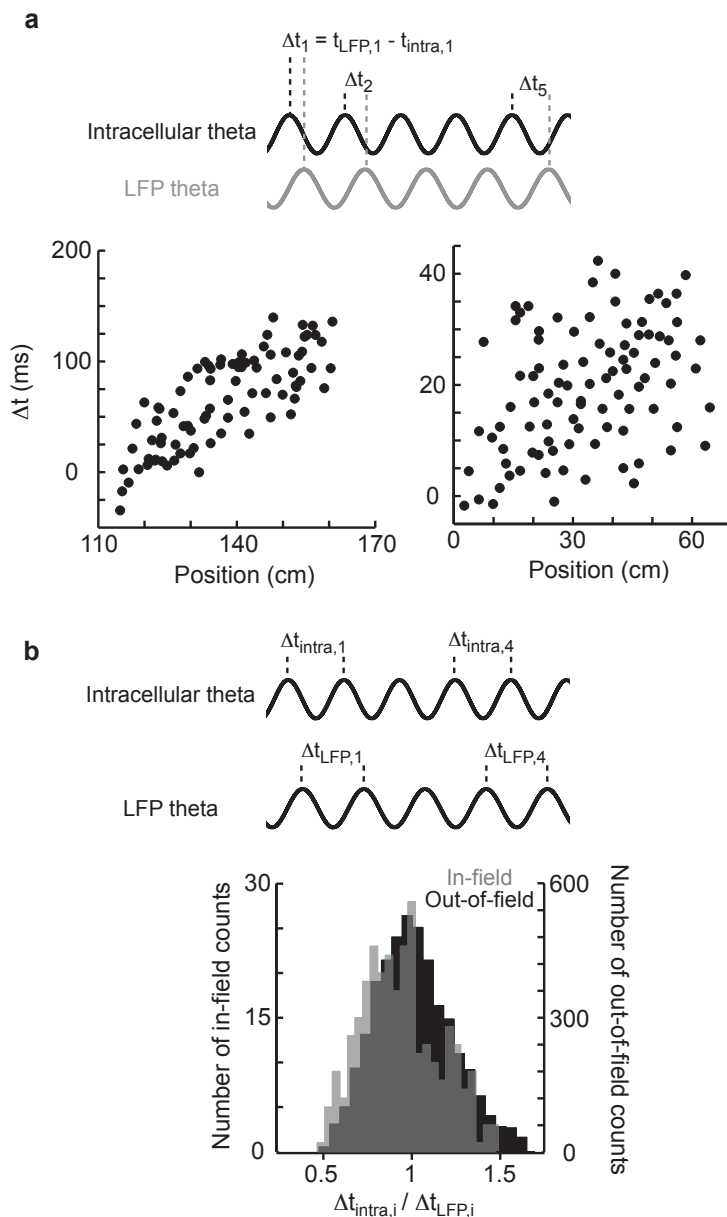
Supplementary Figure 8 | Spectral analysis of intracellular membrane potential recordings. **a**, Example power spectrum from a single cell for epochs inside (black) and outside (red) the place field. Spectra were obtained using multi-taper spectral analysis. **b**, Ratio of power during epochs inside the place field to power during epochs outside the place field for bands from 6-10 Hz and 16-20 Hz. Power increased selectively in the theta-band during epochs inside the place field. Error bars indicated mean \pm sem. n = 8 cells from 8 mice.



Supplementary Figure 9 | Firing rate and theta power maps for non-place cells. **a**, Firing rate maps from intracellular recordings for three putative CA1 pyramidal neurons without place fields. Bottom, vertical lines mark the location along the track of every action potential in the recording. **b**, Power in the theta-frequency band sorted by position along the track for the cells from (a). Power was measured as the squared amplitude of the filtered (6–10 Hz) membrane potential trace.

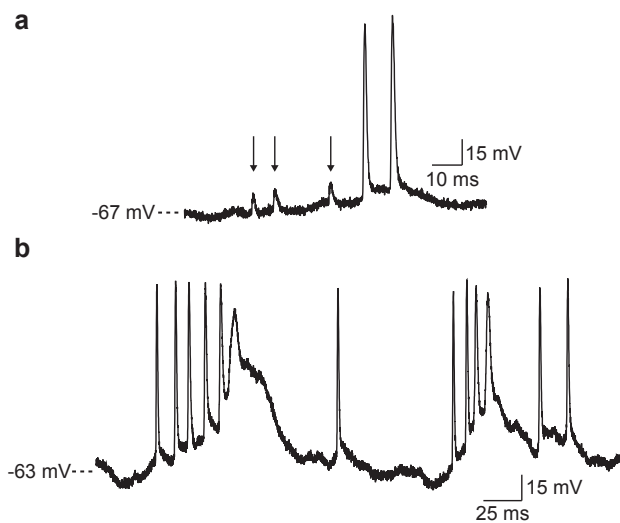


Supplementary Figure 10 | LFP theta oscillations. **a**, Example LFP recording filtered between 2 Hz and 10 kHz. **b**, Two examples of theta power maps from LFP recordings. Theta power was measured as the squared amplitude of the LFP trace filtered between 6–10 Hz. LFP theta power was similar at all locations along the virtual track.



Supplementary Figure 11 | Frequency comparison of intracellular theta oscillations and LFP theta fluctuations from simultaneous LFP and whole cell recordings.

a, Phase shift of intracellular theta oscillations relative to LFP theta oscillations during place field traversals. Δt was defined as the time between the first LFP theta peak in the place field and the first intracellular theta peak, the time difference between the second LFP peak and the second intracellular peak, and so on. Position values are from positions along the virtual track. Examples from 2 cells are shown. **b**, Comparison of the periods of intracellular and LFP theta oscillations. To compare periods in the place field, a ratio of the period of the first intracellular theta oscillation to the period of the first LFP theta oscillation, the ratio of the period of the second intracellular oscillation to the period of the second LFP oscillation, and so on were calculated. Segments of length 3 seconds were analyzed for times outside the place field. Data are from 2 cells from 2 mice.



Supplementary Figure 12 | Example subthreshold phenomena from whole cell recordings. a, Brief, small amplitude spikelets are marked by arrows. **b,** Bursts of action potentials were in some cases followed by prolonged depolarization with broadened action potentials.